Thermal, structural, and orientational relaxation of supercooled salol studied by polarization-dependent impulsive stimulated scattering

C. Glorieux[a)] and K. A. Nelson
Department of Chemistry, Massachusetts Institute of Technology, Cambridge, Massachusetts 02139

G. Hinze[b)] and M. D. Fayer
Department of Chemistry, Stanford University, Stanford, California 94305

Time-resolved transient grating experiments with various polarizations are used to separate different responses and measure their dynamics in supercooled liquid salol. A contribution to signal from orientational alignment induced by flow that arises from thermal expansion is demonstrated. This contribution is distinct from that due to orientational alignment induced directly by the excitation light through the molecular polarizability anisotropy (i.e., through the optical Kerr effect). It is also distinct from signal contributions due to density modulations induced by thermal expansion. The results offer additional insight into salol dynamics and into time-dependent transient grating measurements of this class. Depending on the light polarizations used, any of the signal contributions can be eliminated or highlighted. © *2002 American Institute of Physics.*
[DOI: 10.1063/1.1445749]

I. INTRODUCTION

In recent years, time-dependent optical spectroscopy has yielded extensive contributions to our understanding of complex relaxation in supercooled liquids. Nonresonant transient birefringence (TB) and transient grating (TG) measurements have revealed detailed information concerning the temperature-dependent dynamics of molecular orientation, density, and thermal diffusion. The results have been compared in detail to phenomenological and first-principles formulations of supercooled liquid dynamics.[1–10]

Recently it was discovered that despite their extensive use, TB measurements from supercooled liquids contained contributions to signals that had not been appreciated earlier.[2,11] It was noted that the time-dependent responses observed varied significantly depending on the relative positions of the excitation and probe beams in the sample, suggesting important effects due to mass or thermal transport. It was demonstrated that the origin of this effect was molecular orientational alignment induced by flow of material arising from thermal expansion (Fig. 1). Irradiation by the nonresonant excitation light gives rise to weak absorption into vibrational overtones, resulting in mild heating (typically by several millidegrees kelvin) which is greatest at the center of the excitation spot. This leads to thermal expansion, i.e., flow of material radially outward from the center of the excitation region. Through translational–rotational coupling, this in turn results in orientational alignment of asymmetrical molecules.[12] The magnitude and direction of this orientational alignment, which we will refer to as "flow induced,"

vary as a function of position in the sample relative to the center of the excitation region. In contrast, the direction of molecular orientational alignment induced directly by the excitation light through the molecular polarizability anisotropy (i.e., through the optical Kerr effect or OKE—note that we use this term to denote the optical excitation process, not the transient birefringence experimental geometry through which the response is often measured) depends only on the excitation light polarization and is independent of position relative to the center of the excitation spot. Therefore, the superposition of the flow-induced and OKE-induced orientational responses measured in a transient birefringence experiment does depend on probe position. The measurement of flow-induced orientational contributions to signal, labeled "density-induced heterodyne amplified rotational dynamics" (or "DIHARD") is an important advance since it reveals contributions that may be significant in many TB experiments and because it provides a convenient method for determination of translation–rotational coupling strengths in complex materials.

The DIHARD observations suggest that other measurements in which transient, spatially varying heating and thermal expansion play a role may also be sensitive to flow-induced molecular orientational effects. In transient grating experiments with crossed, parallel polarized excitation pulses, diffracted signals arising from spatially periodic heating and thermal expansion have long been recognized.[13,14] An entire class of such measurements, labeled "impulsive stimulated thermal scattering" (ISTS, which also will be used to denote an excitation mechanism rather than the TG experimental geometry itself) and various other names, has been conducted precisely for the purpose of observing the time-dependent density response (thermal and longitudinal acoustic) to sudden, spatially periodic heating at the transient grating peaks.[4,13,15] In many materials, the diffracted signal

[a)]Permanent address: Laboratorium voor Akoestiek en Thermische Fysica, Katholieke Universiteit Leuven, Celestijnenlaan 200D, B-3001 Leuven, Belgium. Electronic mail: christ.glorieux@fys.kuleuven.ac.be
[b)]Current address: Institut für Physikalische Chemie, Johannes Gutenberg-Universität Mainz, Welderweg 15, D-55099 Mainz, Germany
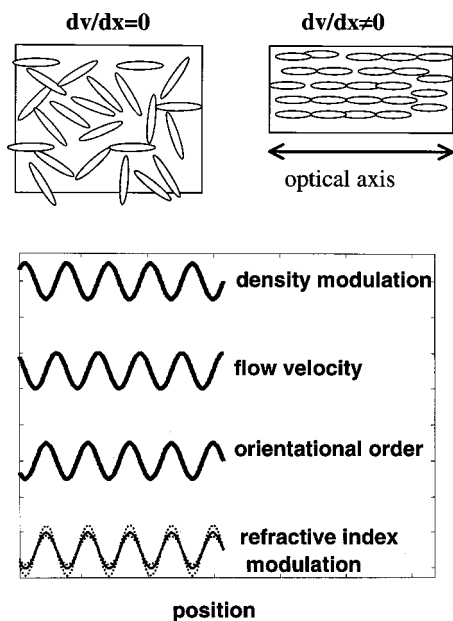
FIG. 1. Flow-induced birefringence. Where a velocity gradient exists, a torque is exerted on anisotropic molecules, resulting in a net alignment and birefringence with the optical axis parallel to the velocity. The bottom plot shows the situation shortly after excitation. The flow velocity amplitude is distributed like the spatial derivative of the density modulation. The induced orientational order evolves like the spatial derivative of the flow velocity, and results in a refractive index modulation which is different (dotted lines) for the two polarizations: $\Delta n_\perp < \Delta n_{iso} < \Delta n_\parallel$.

shows damped time-dependent oscillations due to a transient, longitudinal acoustic response, and shows a nonoscillatory contribution due to steady-state thermal expansion, which eventually decays due to thermal diffusion from the grating peaks to the nulls. In supercooled liquids at some temperatures, a gradual rise of signal level toward the steady-state level is observed, revealing the slow structural relaxation dynamics that mediates thermal expansion. Extensive TG measurements of ISTS-induced density responses have been conducted as a function of transient grating wave vector magnitude q (revealing the q-dependent dispersion in acoustic frequency and damping rate and in the thermal diffusion rate) and as a function of sample temperature.[5] However, flow-induced orientational contributions to TG signals have not been recognized. Their consideration is important to ensure correct analysis of the signals and to provide additional information content of particular interest for supercooled liquids.[2]

Most TG measurements of ISTS-induced density responses have been conducted with both excitation light polarizations either perpendicular to the grating wave vector direction (i.e., with ''vertical'' or ''VV'' excitation polarizations) or in a plane containing the grating wave vector (''HH'' polarizations) and with similar (VV or HH) probe and signal polarizations. The measurements can be denoted ''VVVV,'' ''VVHH,'' ''HHVV,'' and ''HHHH,'' with the two excitation, probe, and signal polarizations listed in order. In these configurations, orientational contributions to signal due to molecular polarizability anisotropy (OKE) are well known.[14] An additional signal contribution due to acoustic waves excited through impulsive stimulated Brillouin scat-

tering (ISBS) may also be observed, especially at large wave vectors.[5,16] In most cases, even modest (mK) heating gives rise to thermally induced ISTS signals (thermal expansion and longitudinal acoustic wave) that are substantially stronger than signal contributions arising from either OKE-induced molecular orientation or ISBS-induced acoustic waves. However, flow-induced molecular orientation is also driven thermally, and the magnitude of the orientational alignment, like the magnitude of the ISTS-induced density response, is assumed to be linearly proportional to the amount of heating.[2] Therefore, flow-induced orientational signal contributions will not be suppressed relative to density contributions on the basis of absorption strength.

TG excitation polarization combinations other than the four discussed above also have been used. The most common alternative employs perpendicularly polarized (''VH'') excitation pulses and perpendicularly polarized (VH) probe and signal beams, yielding the polarization combination denoted ''VHVH.'' In this case, there is no spatially periodic heating of the sample but instead a spatially periodic excitation polarization.[17] OKE excitation in this case leads to molecular orientation with spatially varying magnitude and alignment direction. The orientational relaxation dynamics can be measured through VH probe and signal polarizations. The VHVH configuration permits measurement of OKE-induced orientational relaxation dynamics without any contributions to signal due to density variations or flow-induced orientational alignment.[14] In solids and some supercooled liquids, ISBS-excited transverse acoustic waves may also contribute to the response. The conventional transient birefringence measurement (with the probe beam centered on the excitation region) can be thought of as a VHVH TG measurement in the limit of a zero-degree angle between the pulses. We note that all of the signal contributions discussed thus far—ISTS, ISBS, OKE, and flow-induced—have the same dependence on excitation light intensity, and therefore none can be selectively enhanced or eliminated through variation of the intensity. Therefore, polarization is a particularly important control parameter.

In this paper the contribution of flow-induced molecular orientation to TG signals from a supercooled liquid is explored in detail. Time-dependent orientational signal contributions are identified and measured, and TG polarization combinations that either suppress or highlight flow-induced signals are considered. A detailed theoretical treatment of the TG experiment, including various polarization combinations, all of the excitation mechanisms discussed above, and optical heterodyne detection, is presented in the next section. This is followed by experimental results and comparison to the theoretical expectations. Finally, concluding remarks are offered.

II. CONTRIBUTIONS TO TG SIGNALS

A. Heterodyne TG detection

The signals in our experiments are all measured through optical heterodyne detection[13,18,19] of the diffracted field, as illustrated in Fig. 2. A short pulse is incident on a phase mask, yielding ± 1 orders of diffraction that are used for the
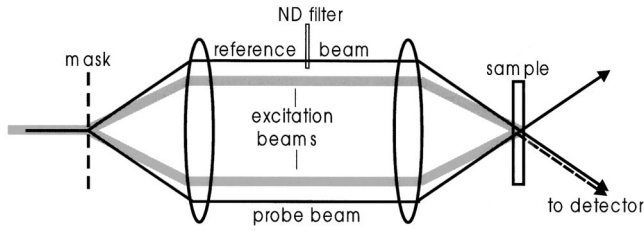
FIG. 2. Optical heterodyne transient grating geometry. Both pump and probe beams are split into ±1 diffraction orders by the phase mask, and the separated beams are recombined at the sample. The diffracted signal beam is coincident and phase coherent with, and thus amplified by, the reference beam. Polarization optics is inserted into the incident and signal beam paths to select specified signal components.

two excitation pulses. A different wavelength cw or quasi-cw beam of intensity I_{in} is incident on a mask with the same spatial period as the first, and the ±1 orders of diffraction produced with phase mask diffraction efficiency ε are used for the probe and reference beams. The reference beam is partially attenuated by a neutral density filter, leaving reference beam intensity $\eta \varepsilon I_{in}$, to optimize signal and signal/noise levels. The detected intensity can be expressed as

$$I = E_{dif}^2 + E_{ref}^2 + E_{dif}E_{ref}\cos\phi = (\zeta\varepsilon I_{in} + \eta\varepsilon I_{in}$$
$$+ \varepsilon\sqrt{\zeta\eta I_{in}I_{in}}\cos\phi)/2, \qquad (1)$$

with ϕ the optical phase between the diffracted beam and the reference beam and $\zeta(t)$ the time-dependent sample diffraction efficiency. $\eta = 0$ corresponds to homodyne detection. Heterodyne detection $(0 < \eta < 1)$ has two main advantages. The mixing term, which gives the largest time-dependent contribution to the signal, is linear with respect to the sample response (i.e., to the induced refractive index changes of the sample, which themselves are linearly proportional to the excitation-induced density and orientational responses, the excitation-induced temperature changes, and the excitation light intensity), simplifying the analysis. In addition, the magnitude of η can be optimized to render the best compromise between a large signal (compared to electronic detector noise) and a moderate dc signal background E_{ref}^2 with its accompanying optical noise. In cases where the homodyne contribution to the signal is not negligible, data can be obtained with positive and negative $\cos\phi$. The difference signal is free of not only the homodyne contribution but also of contributions due to heterodyne mixing between the signal and parasitically scattered probe light and of synchronized spurious noise contributions that may be associated with the firing of the pump laser (e.g., electromagnetic pickup resulting from switching of a Pockels' cell). Heterodyne detection is also versatile in cases where the signal polarization is of importance. By choosing the appropriate reference beam polarization, a specific diffracted beam polarization component can be selectively amplified.

B. Optically isotropic and anisotropic signal contributions

We will be treating isotropic samples, with density ρ and refractive index $n_{iso}(\rho)$, in which transient optical anisotropy may be induced through partial molecular orientational

alignment. The partially aligned system is uniaxial, with refractive index components perpendicular and parallel to the alignment direction given by

$$n_\perp^2(x,t) = n_{iso}^2(\rho(x,t)) - \tfrac{1}{3}S(x,t)\Delta\varepsilon + \Delta n_{P,\perp}^2$$
$$n_\parallel^2(x,t) = n_{iso}^2(\rho(x,t)) + \tfrac{2}{3}S(x,t)\Delta\varepsilon + \Delta n_{P,P}^2, \qquad (2)$$

with $\Delta\varepsilon$ the maximum anisotropy (all molecular axes oriented parallel with optical axis) of the dielectric permittivity and $S(t) \equiv \langle P_2[\cos\theta(t)]\rangle$ (θ is the angle of the molecular axis with the optical axis) the order parameter characterizing the degree of macroscopic anisotropy. The density dependence of the refractive index could be calculated approximately through the Clausius–Mossotti relation $(\varepsilon_r - 1)/(\varepsilon_r + 2) = \rho N_A \alpha/m_M\varepsilon_0$, with ρ the density, N_A Avogadro's number, m_M the molar mass, $\varepsilon_r = n_{iso}^2$ the relative dielectric permittivity, ε_0 the dielectric permittivity of vacuum, and α the molecular polarizability. $\Delta n_{P,\perp}$ and $\Delta n_{P,\parallel}$ are the stress (P) induced birefringence contributions to the respective refractive index components, which are due to anisotropic refractive index changes without molecular alignment. To a large extent these contributions play a minor role in the analysis. Therefore, for the time being, we will omit them, and postpone the discussion of their relevance to Sec. III.

In this section we consider orientational alignment due to flow only.[2,14,15,20] In this case the alignment direction is parallel to the "horizontal" (H) transient grating wave vector direction. The refractive index for V-polarized (ordinary wave) light is then $n_\perp$ and for H-polarized light is $n_\parallel$. Note that we generally use "H" polarization to refer to beams polarized in a plane that includes the grating wave vector and the bisector of the excitation beams, so only in the limit of small scattering angles does the polarization direction approach the wave vector direction. In general, the refractive index for this extraordinary H polarization electric field component is given by $n_{extra}^2 = n_\parallel^2 n_\perp^2/(n_\parallel^2\sin^2\theta + n_\perp^2\cos^2\theta)$, with θ the angle between the probe beam wave vector and the optical axis. However, most TG measurements are conducted with modest scattering angles, and the small refractive index variation for H-polarized beams will be neglected.

Equation (2) implies that the ordinary and extraordinary wave component of the incident electric field are diffracted with different efficiencies. The induced optical axis (OA) is chosen as the reference x axis (in practice horizontal) for the angles. Assume the incident probe light has a polarization α, i.e., the electric field vector makes an angle α with the optical axis and is given by $\mathbf{E}_p = (\cos\alpha, \sin\alpha, 0)$. The ordinary component $\mathbf{E}_{ord}$ of the electric field generates diffracted light with amplitude

$$E_x = gE_{p,ord}(\Delta n_{iso} - \tfrac{1}{3}S\Delta\varepsilon) = gE_p\sin\alpha(\Delta n_{iso} - \tfrac{1}{3}S\Delta\varepsilon), \qquad (3)$$

with g a geometrical proportionality factor.

The extraordinary component $\mathbf{E}_{extra}$ of the electric field generates diffracted light with amplitude

$$E_y = gE_{p,extra}(\Delta n_{iso} + \tfrac{2}{3}S\Delta\varepsilon)$$
$$= gE_p\cos\alpha(\Delta n_{iso} + \tfrac{2}{3}S\Delta\varepsilon). \qquad (4)$$

J. Chem. Phys., Vol. 116, No. 8, 22 February 2002

Relaxation of supercooled salol   3387

The analyzing polarizer makes an angle β with the optical axis, and acts as a projection operator $\mathbf{u}(\cos\beta, \sin\beta, 0)$. The diffracted field that is transmitted through the polarizer and reaches the detector, E_{sig}, is given by the projection of $(E_x, E_y, 0)$ on $\mathbf{u}$

$$E_{\text{sig}} = E_p \cos\alpha \cos\beta (\Delta n_{\text{iso}} + \tfrac{2}{3} S \Delta\varepsilon)$$
$$+ E_p \sin\alpha \sin\beta (\Delta n_{\text{iso}} - \tfrac{1}{3} S \Delta\varepsilon). \quad (5)$$

The signal field component E_ρ due to the density change is given by

$$E_\rho = E_p (\cos\alpha \cos\beta + \sin\alpha \sin\beta) \Delta n_{\text{iso}}. \quad (6)$$

The signal field component E_{rot} due to flow-induced orientation is given by

$$E_{\text{rot}} = E_p (2 \cos\alpha \cos\beta - \sin\alpha \sin\beta) \frac{S\Delta\varepsilon}{3}. \quad (7)$$

From Eqs. (5)–(7), two special cases can be deduced. The flow-induced orientational contribution to signal can be eliminated and the pure density contribution[2] maximized by choosing $\alpha = \beta = 54.74°$ so that $2\cos\alpha\cos\beta - \sin\alpha\sin\beta = 0$ and $E_{\text{sig}} = E_\rho = E_p \Delta n_{\text{iso}}$. Note that the density contribution to signal can be isolated without any reduction in its intensity relative to the usual HH or VV probe and signal polarizations.

On the other hand, a maximum pure rotation-induced signal[2] can be obtained by choosing $\alpha = \beta = 45°$ so that $(\cos\alpha\cos\beta + \sin\alpha\sin\beta) = 0$ and $E_{\text{rot}} = -E_P S\Delta\varepsilon/2$.

C. Signal sources

The mild optical absorption of two horizontally crossed pump laser beams results in a grating-like heat source $Q(x,t) = Q_0 \cos(q_0 x) f(t) g(x)$, with $q_0 = 2\pi/\Lambda$, $\Lambda = \lambda/[2\sin(\theta/2)]$ the grating spacing, λ the optical wavelength, and θ the crossing angle. For our purposes, $f(t)$, the temporal envelope of the laser pulse (of the order of 300 ps length) can be considered as a delta function. In what follows, $g(x)$, the slowly varying (compared to Λ) Gaussian envelope of the pump beam shape, will be treated as uniform. In the wave vector-time domain this corresponds to $Q(q,t) = Q_0 \delta(q = q_0) \delta(t=0)$, with q the wave vector. The details of the y- and z dependence of Q are not essential for this outline.

By combining the longitudinal part of the Navier–Stokes equation[4]

$$\rho_0 \frac{\partial}{\partial t} v_\parallel(q,t) - iq \frac{k_B T_0}{S(q)} \delta\rho(q,t) - iq \frac{k_B T_0}{S(q)} \rho_0 \kappa \delta T(q,t)$$
$$+ \rho_0 q^2 \int_0^t dt' \, \phi_L(q, t-t') v_\parallel(q,t') = iq F(q,t), \quad (8)$$

the continuity equation

$$\frac{\partial}{\partial t} \rho(q,t) - \rho_0 i v_\parallel(q,t) = 0, \quad (9)$$

the energy transport equation,

$$\rho_0 c_v \frac{\partial}{\partial t} \delta T(q,t) - c_v \frac{\gamma-1}{\kappa} \frac{\partial}{\partial t} \rho(q,t) + \kappa_{\text{th}} q^2 \delta T(q,t)$$
$$= Q(q,t), \quad (10)$$

and assuming Debye relaxation

$$\phi_L(q,t) = \nu_L + \phi_L^R(q,t) = \nu_L + \nu_R \exp(-t/\tau_R) \quad (11)$$

for the memory function ϕ_L in Eq. (8) (ν_L is the longitudinal kinematic viscosity, ν_R the Debye relaxation time) and approximating for the small wave vector limit, one arrives at a 2×2 matrix equation in temperature and density, and finally at the dispersion equation for thermal diffusion, longitudinal acoustic propagation, and structural relaxation[4]

$$(s + \Gamma_{\text{th}})(s + i\omega_{\text{ac}} + \Gamma_{\text{ac}})(s - i\omega_{\text{ac}} + \Gamma_{\text{ac}}) \left[s + \frac{c_0^2}{c_\infty^2 \tau_R} \right] = 0, \quad (12)$$

in the time-conjugate Laplace variable $s = i\omega$, corresponding to a time-domain density response

$$S_{\text{dens}} \propto A \left(\exp\left(-\frac{t}{\tau_{\text{th}}}\right) - \exp\left(-\frac{t}{\tau_{\text{ac}}}\right) \cos(2\pi f_{\text{ac}} t) \right)$$
$$+ B \left(\exp\left(-\frac{t}{\tau_{\text{th}}}\right) - \exp\left(-\frac{t}{\tau_{\text{st}}}\right)^\beta \right). \quad (13)$$

In the above equations, ρ_0 is the steady-state density, $v_\parallel$ the particle velocity, κ the thermal expansion coefficient, $\gamma = c_p/c_v$, c_p and c_v the specific heat capacity at constant pressure and volume, respectively, κ_{th} the thermal conductivity, ϕ_L the memory function, $S(q)$ the static structure factor, and k_B the Boltzmann constant. $F(q,t)$ is the electrostrictive driving force. c_0 and c_∞ are, respectively, the zero frequency and infinite frequency limits of the longitudinal sound velocity. $f_{\text{ac}} = \omega_{\text{ac}}/(2\pi)$ is the acoustic frequency, $\tau_{\text{th}} = \Gamma_{\text{th}}^{-1}$, $\tau_{\text{ac}} = \Gamma_{\text{ac}}^{-1}$, τ_{st} are the thermal, acoustic, and structural relaxation times, respectively, and β is the stretched exponential exponent. Details of this derivation and the expressions for A and B are given in Yang and Nelson.[4–6] As mentioned before, the density grating response S_{dens} is coupled via the Clausius–Mossotti relation to n_{iso}, causing diffraction of the probe beam. The ad hoc modification of Eq. (13) with an exponent β different from unity permits non-Debye-type structural relaxation in general to be treated. Stretched exponential (Kohlrausch–Williams–Watts or KWW) behavior of the structural relaxation, which here is probed via the density relaxation (Mountain mode),[21,22] is found in many experiments on supercooled liquids.[23]

An important feature of experimental data described by Eq. (13) is the Debye–Waller factor, which is determined by the ratio B/A. Mode coupling theory (MCT) for supercooled liquids predicts a characteristic temperature dependence of this "nonergodicity parameter".[20,24] To determine the nonergodicity parameter associated with structural relaxation, the time scales for acoustic oscillations, structural relaxation, and thermal diffusion have to be well separated, i.e., $\tau_{\text{ac}} \ll \tau_{\text{st}} \ll \tau_{\text{th}}$.

The density gradient caused by both the initial, net flow of molecules out of the heated regions and the passage of the spatially and temporally periodic acoustic wave afterwards, results in a flow

$$v_\parallel(q,t) = \frac{1}{i\rho_0}\frac{\partial}{\partial t}\rho(q,t) \tag{14}$$

and a flow gradient

$$\frac{\partial v_\parallel(q,t)}{\partial x} = \frac{1}{i\rho_0}\frac{\partial}{\partial x}\frac{\partial}{\partial t}\rho(q,t) = \frac{q}{\rho_0}\frac{\partial}{\partial t}\rho(q,t). \tag{15}$$

Through translational–rotational coupling, measured by the coupling parameter $\gamma_{\text{tr–rot}}$, material flow drives the molecular orientational response $S_{\text{flow}}(t)$.

The coupling, described by the relation[12,25]

$$\frac{\partial S_{\text{flow}}}{\partial t} + \frac{S_{\text{flow}}}{\tau_{\text{or}}} = \gamma_{\text{tr–rot}}\frac{\partial v_\parallel}{\partial x}, \tag{16}$$

and acting through the time-dependent flow gradient

$$\begin{aligned}
\frac{\partial v_\parallel}{\partial x} &= \frac{q}{\rho_0}\frac{\partial}{\partial t}\rho(q,t) \\
&= \frac{q}{\rho_0}\frac{\partial}{\partial t}\left(A\left(\exp\left(-\frac{t}{\tau_{\text{th}}}\right) - \exp\left(\left(i2\pi f_{\text{ac}} - \frac{1}{\tau_{\text{ac}}}\right)t\right)\right)\right. \\
&\quad \left. + B\left(\exp\left(-\frac{t}{\tau_{\text{th}}}\right) - \exp\left(-\frac{t}{\tau_{\text{st}}}\right)^\beta\right)\right) \\
&= -\frac{q}{\rho_0}\left(\left(\frac{A}{\tau_{\text{th}}}\exp\left(-\frac{1}{\tau_{\text{th}}}\right) - A\left(i2\pi f_{\text{ac}} - \frac{1}{\tau_{\text{ac}}}\right)\right.\right. \\
&\quad \left.\times\exp\left(\left(i2\pi f_{\text{ac}} - \frac{1}{\tau_{\text{ac}}}\right)t\right)\right) + \left(\frac{B}{\tau_{\text{th}}}\exp\left(-\frac{t}{\tau_{\text{th}}}\right)\right. \\
&\quad \left.\left. -\frac{\beta B}{\tau_{\text{st}}}\left(\frac{t}{\tau_{\text{st}}}\right)^{\beta-1}\exp\left(-\frac{t}{\tau_{\text{st}}}\right)^\beta\right)\right),
\end{aligned} \tag{17}$$

drives a molecular orientational response given by

$$\begin{aligned}
S_{\text{flow}}(q,t) &\propto C\exp\left(-\frac{t}{\tau_{\text{ac}}}\right)\cos(2\pi f_{\text{ac}}t) \\
&\quad + D\exp\left(-\frac{t}{\tau_{\text{or}}}\right)^{\beta_{\text{or}}} + E\exp\left(-\frac{t}{\tau_{\text{th}}}\right) \\
&\quad + F\exp\left(-\frac{t}{\tau_{\text{st}}}\right) + G\exp\left(-\frac{t}{\tau_{\text{st}}}\right)^\beta \\
&\quad + H\exp\left(-\frac{t}{\tau_{\text{st}}}\right)^\beta \otimes \exp\left(-\frac{t}{\tau_{\text{or}}}\right)^{\beta_{\text{or}}}.
\end{aligned} \tag{18}$$

Each driving term in Eq. (17) contributes to the flow response in Eq. (18). In general, an exponentially decaying driving term $K\exp(-t/\tau)$ in Eq. (16) leads to a response of the form

$$S_G(t) \propto \frac{K}{\left(\dfrac{1}{\tau_{\text{or}}} - \dfrac{1}{\tau}\right)}(\exp(-t/\tau) - \exp(-t/\tau_{\text{or}})). \tag{19}$$

Equation (19) shows that the response to a driving force with a decay time substantially slower than the orientational relaxation time decays with essentially that decay time. When the driving force is fast compared to orientational relaxation, the response is an exponential decay with the orientational relaxation time. The stretched exponential driving term acts more or less as an exponential driving force faster than $\exp(-t/\tau_{\text{st}})$ for $t < \tau_{\text{st}}$ and slower than $\exp(-t/\tau_{\text{st}})$ for $t > \tau_{\text{st}}$. According to Eq. (17) fast driving terms dominate the response since the amplitude of each term is given by the time derivative of the density.

At high temperatures, where structural relaxation is fast and there is no gradual rise of the density response, the initial thermal expansion density jump gives a delta function contribution to the velocity gradient yielding an $\exp(-t/\tau_{\text{or}})$ term which dominates the more slowly decaying term from thermal diffusion. Together with the response to the oscillating acoustic driving term, this yields a simplified orientational response

$$S_{\text{flow}} \propto C\exp\left(-\frac{t}{\tau_{\text{ac}}}\right)\cos(2\pi f_{\text{ac}}t) + D\exp\left(-\frac{t}{\tau_{\text{or}}}\right)^{\beta_{\text{or}}}. \tag{20}$$

In analogy to the density response, we have generalized the orientational response to a stretched exponential form with relaxation time τ_{or} and stretching exponent β_{or}. At lower temperatures, structural relaxation becomes slower and a gradual density change is clearly observable on time scales longer than the acoustic oscillation period. In this case Eq. (18) can be expected to evolve to

$$S_{\text{flow}} \propto C\exp\left(-\frac{t}{\tau_{\text{ac}}}\right)\cos(2\pi f_{\text{ac}}t) + D'\exp\left(-\frac{t}{\tau'}\right)^\beta, \tag{21}$$

where τ' and β represent an approximate convolution of the structural and orientational relaxation stretched exponential parameters, respectively, resulting from a driving function which is a product of a stretched exponential (with the structural relaxation parameters) and $t^{(\beta-1)}$ factor (with a fractional negative exponent) and a response function which is another stretched exponential (with the orientational relaxation parameters). While our simplification of this part of the response is clearly a crude approximation, we anticipate that this is a small part of the total response in all cases since the density response is slow and its time derivative, which gives the orientational driving force, is small. Our objective here is to allow for a relatively simple phenomenological description of the slow dynamics without undue emphasis on its details, the determination of which will be beyond our experimental ability. Indeed, our primary objective in considering the slow flow-induced orientational response will be to estimate the relative magnitude of its contribution to ISTS signals, rather than to determine its precise dynamics.

The amplitude factors C and D (or D') are determined by the driving source (acoustic wave oscillations and initial

net outflow, respectively) and by the translational–rotational coupling factor $\gamma_{\text{tr–rot}}$. In principle, Eqs. (20) and (21) allow determination of the orientational relaxation parameters τ_{or} and β_{or} and the coupling parameter $\gamma_{\text{tr–rot}}$. The orientational response S_{flow} is equal to the orientational order parameter in Eqs. (2)–(7). The net molecular flow corresponding to the "dc" part (before thermal diffusion sets in) of the thermal expansion in the case of very slow responses gives rise to a net contribution of rotational relaxation to the signal. Under some circumstances, the relatively large strength of the anisotropic signal facilitates study of rotational relaxation, especially in cases where the OKE excitation (neglected in this treatment) efficiency is small.[2] According to Eq. (21) molecular flow also oscillates synchronously with passing longitudinal acoustic waves, giving an oscillating contribution.

D. Signal contribution selection schemes

We now consider explicitly the VVVV, HHHH, VVHH, and HHVV polarization combinations used experimentally.[2] In our experiments, ISTS excitation yielded the predominant signals. Still, OKE signal contributions are easily treated and will be considered below. With the polarization combinations used, the OKE-induced orientational alignments are along the V or H directions, and so the birefringence $\Delta\varepsilon = \varepsilon_\parallel - \varepsilon_\perp$ is defined with respect to the same coordinate axes as that due to flow-induced orientation (which is the horizontal H direction). However, the magnitude and time dependence of the orientational alignments, as described by $S(x,t)$, are very different. For the polarization combinations under consideration, we obtain the following results for the signal intensities (which are linearly proportional to the refractive index variations):

$$I_{HHHH} = \delta(n_{\text{iso}}^2 + \tfrac{2}{3}S_{\text{flow}}\Delta\varepsilon + \tfrac{2}{3}S_{\text{Kerr}}\Delta\varepsilon)^{1/2}$$

$$I_{HHVV} = \delta(n_{\text{iso}}^2 - \tfrac{1}{3}S_{\text{flow}}\Delta\varepsilon - \tfrac{1}{3}S_{\text{Kerr}}\Delta\varepsilon)^{1/2}$$

$$I_{VVHH} = \delta(n_{\text{iso}}^2 + \tfrac{2}{3}S_{\text{flow}}\Delta\varepsilon - \tfrac{1}{3}S_{\text{Kerr}}\Delta\varepsilon)^{1/2}, \tag{22}$$

$$I_{VVVV} = \delta(n_{\text{iso}}^2 - \tfrac{1}{3}S_{\text{flow}}\Delta\varepsilon + \tfrac{2}{3}S_{\text{Kerr}}\Delta\varepsilon)^{1/2}$$

leading, after a first-order expansion (the refractive index changes are much smaller than unity) to the interesting signal subtraction schemes

$$I_\rho = \tfrac{1}{3}(I_{HHHH} + 2I_{HHVV})$$
$$= \tfrac{1}{3}(I_{HHVV} + I_{VVHH} + I_{VVVV})$$
$$= \tfrac{1}{3}(-I_{HHHH} + 2I_{VVHH} + 2I_{VVVV})$$
$$= \tfrac{1}{3}(3I_{HHHH} + 4I_{HHVV} - 2I_{VVHH} - 2I_{VVVV}),$$

$$I_{\text{or,flow}} = I_{HHHH} - I_{VVVV} = I_{VVHH} - I_{HHVV}, \tag{23}$$

$$I_{\text{or,Kerr}} = I_{HHHH} - I_{VVHH} = I_{VVVV} - I_{HHVV}.$$

For maximum signal, the polarization of the heterodyne-amplifying reference beam is always chosen parallel with the analyzing output polarizer.

Note that in Eq. (22), while the OKE part of the signal fulfills the symmetry conditions well known for four-wave mixing experiments[26,27] (e.g., I_{VVHH} can be identified with I_{xxyy} in the conventional notation in the laboratory frame of

four-wave mixing), the flow-induced part of the signal does not. This is easily understood since the heating of the sample occurs through absorption of the excitation pulses, and their absorption by the isotropic sample is polarization independent. This heating results in mass flow whose direction depends on the grating wave vector direction ("H" as defined in the present case), i.e., on the excitation geometry but not on the excitation polarization, as long as the excitation pulses are polarized parallel to each other. The flow-induced molecular orientational alignment is parallel to the flow direction, again dependent on the excitation geometry but not on the excitation polarization. Finally, the flow-induced molecular orientational alignment results in diffracted signal whose intensity is dependent on the probe polarization. Thus, for example, signals I_{HHHH} and I_{VVVV} (all H polarizations and all V polarizations, respectively) are different, signals I_{HHHH} and I_{HHVV} (H excitation polarization and H or V probe polarization, respectively) are different, while signals I_{VVHH} and I_{HHHH} (H or V excitation polarization and H probe polarization) are the same since the signals depend on the choice of probe but not excitation polarization. More generally, the effects of flow on light scattering and its polarization dependences has been treated in detail theoretically.[28–30]

III. EXPERIMENTAL RESULTS AND DISCUSSION

The sample was excited by the output of a Q-switched, mode-locked, cavity-dumped Nd:YAG laser (pulse duration 300 ps, pulse energy 500 μJ, repetition rate 50 Hz, wavelength 1064 nm) and the refractive index effects were probed by a cw laser diode (power 70 mW, wavelength 830 nm). The pump light at 1064 nm is weakly but sufficiently absorbed by salol (phenyl salicylate) due to an overtone of the OH stretching mode. The diffracted light was detected by a combination of a fast (ac-coupled) Hamamatsu C5658 detector ($1\,\text{ns} < t < 2\,\mu\text{s}$) and a slower (dc-coupled) New Focus No. 1801 detector ($t > 2\,\mu\text{s}$). An *ad hoc* visual optimization of the match between the fast and slow detector signals was done by multiplying one of them with an appropriate factor. The phase masks used in the heterodyne diffraction setup had a diffraction efficiency of typically 30% into each of the two first orders. We used grating spacings of 16 μm and 52 μm, corresponding with scattering angles of 1.9°, respectively, 1.0°. The reference probe beam was attenuated 450 times by a neutral density filter, which also was tilt controlled to manipulate the optical phase ϕ [see Eq. (1)]. The temperature was controlled by a Lakeshore model 330 controller, which kept the temperature stable within 0.1 K during each experiment. The temperature of the quartz sample cuvette was detected by a platinum thermistor attached to the cuvette using thermally conducting paste. The polarizations of the two pump and two probe beams were individually controlled by Glan-Taylor polarizers (extinction ratio 10^{-5}) which were mounted on a combined tilt and rotation stage that was carefully adjusted to avoid beam walk during polarization rotation. Typically, data were averaged over 4096 laser shots.

Figure 3 shows three typical signals obtained in heterodyne and homodyne diffraction modes. The middle trace, the
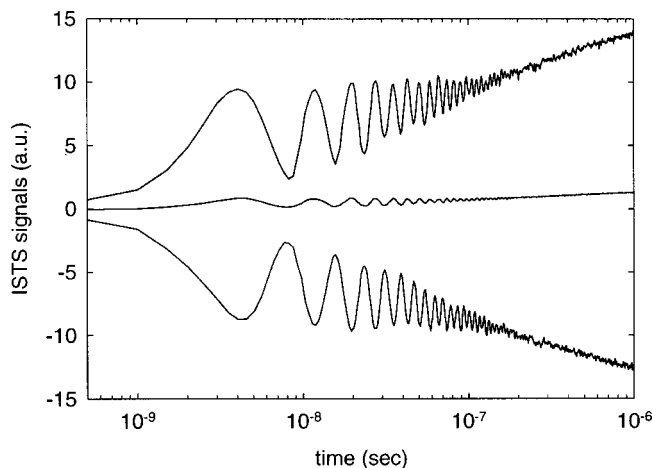
FIG. 3. TG signals (16 μm grating, HHHH) obtained from salol at 245 K. The middle trace shows homodyne signal, while the upper and lower traces show heterodyned signals with the reference phase optimized for constructive (upper trace) or destructive (lower trace) interference between the reference and diffracted fields.

FIG. 4. Heterodyne TG signal intensity from salol at 245 K, with a 52-μm grating fringe spacing. The acoustic oscillations appear on relatively fast (nanosecond) time scales. Complex, nonexponential structural relaxation dynamics on submicrosecond time scales gives rise to the gradual increase in signal, as the density modulation of the sample due to spatially periodic heating gradually reaches steady state. On an even longer time scale (not shown), thermal diffusion equilibrates the grating peak and null temperatures and returns the signal level to zero. The difference between HHHH and HHVV signals reveals the presence of an orientational contribution. The steady-state signal levels have been set equal so that the complex relaxation dynamics leading to them could be compared for the different polarization combinations.

homodyne signal, was obtained without the reference beam, while the other two signals were obtained using the reference beam with $\cos \phi = 1$ (top) and $\cos \phi = -1$ (bottom). The signals illustrate that for the optimized value of $\eta = 1/450$ in this case (minimizing the combination of optical and electronic detector noise), the heterodyne gain is significant: the heterodyned signal intensity is about 11 times larger than the homodyne signal intensity. From this, we can conclude that the maximum diffraction efficiency I_D/I_0 of the induced grating was about 2×10^{-5}. Using an approximate expression[27] for the diffraction efficiency $I_D/I_0 = |\pi \Delta n d/\lambda|$ of a refractive index grating over a depth $d = 4$ mm ($d =$ depth of focus of our crossing pump beams, $\lambda = 1.064$ μm is the pump beam wavelength), this corresponds to a maximum refractive index variation $\Delta n = 4 \times 10^{-7}$.

The signals in Fig. 4, obtained with different polarization combinations of pump and probe, are dominated by the density response. However, significant differences among the signals (whose steady-state levels have been set at the same value at $t > 2 \cdot \mu$s) are due to different orientational contributions. The orientational and density dynamics are clearly different since the time dependence of the signal changes when different polarization combinations which allow more or less orientational contribution are used. Differences of up to 30% in the relative signal levels at various times are observed from the data. As discussed above, orientation and density contributions can be extracted from the data either by combining data from several experiments through Eq. (23) or by single experiments using certain polarization configurations. Figure 5 illustrates the signals with and without the orientational contribution. The upper and lower traces show the results of HHHH and VVHH experiments. The middle trace is the (55°,55°) (magic angle configuration) experimental result along with calculated pure density signal (dashed trace) based on the HHHH and HHVV signals and Eq. (5). The experimental and calculated curves are well matched. A correction factor of 0.92, compensating for a slight heterodyne mismatch (caused by imperfect reference phase optimization
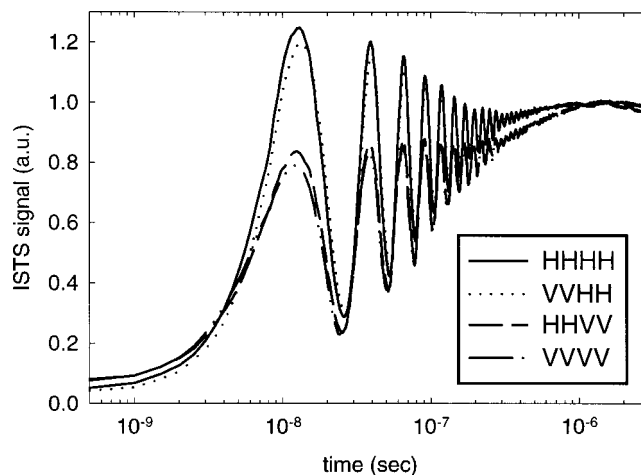
in the different experimental signals), was used to match the experimental and calculated 55°,55° signal intensities as well as possible. This factor does not influence the dynamical features of the data, which match well without any adjustable parameters.

A similar approach can be applied to obtain the pure orientational contribution. Figure 6 illustrates the analyzer polarization dependence of the diffracted signal for 45° inci-
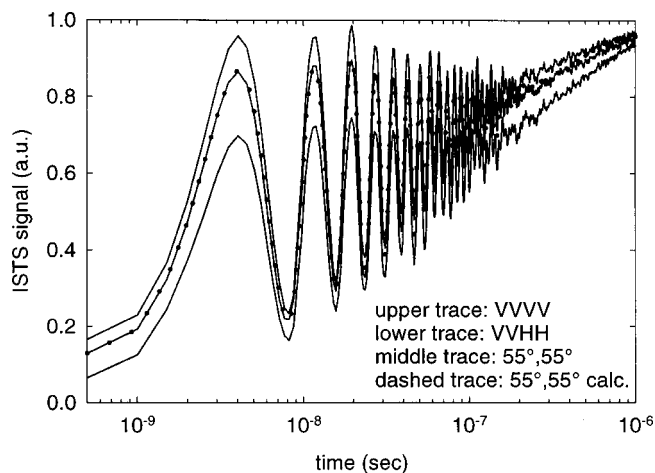

FIG. 5. Illustration of the orientational contribution to ISTS signals detected in HHHH and HHVV configurations (upper and lower traces, respectively) at 245 K, with a 16-μm grating spacing. The middle trace is the 55°,55° (magic angle configuration) experimental curve along with calculated signal due to density only [dotted trace, based on Eq. (23) and the HHHH and HHVV signals]. A correction factor of 0.92, compensating for imperfect heterodyne phase optimization in the experimental signals, was used to match the experimental and calculated 55°,55° signal intensities as well as possible.
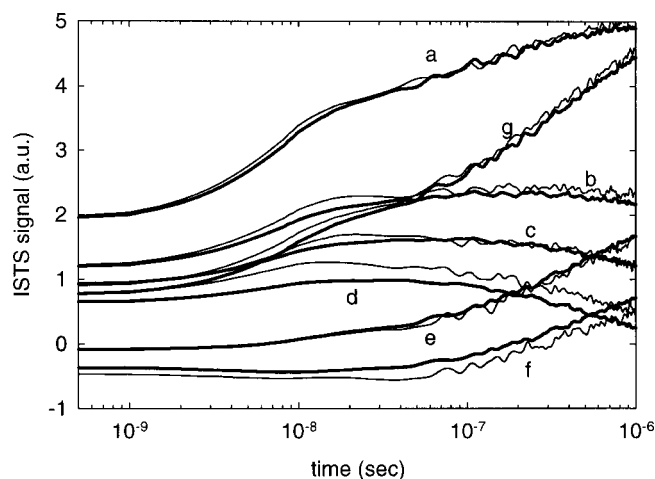
FIG. 6. Illustration of the polarization (θ) dependence of the diffraction signal at 245 K, 16-μm grating. The curves plotted with thin lines are obtained from the experiment. The incident polarization angle for all signals was 45°, the analyzing polarization angle was −70° (a), −55° (b), −50° (c), −45° (d, "magic angle" combination), −35° (e), and −20° (f). The bold curves are calculated using Eq. (23) from the HHHH and HHVV signal for the 45°,θ magic angle configuration. To enhance the visibility of other features, the acoustic responses are suppressed using a 10 ns Gaussian smoothing filter. A global multiplicative correction factor was used to match the curves as well as possible. Small differences between theory and experiment are likely due to the imperfect manual optimization of the individual heterodyne phases.

FIG. 7. Flow-induced orientational response at 252 K, 52 μm grating spacing, obtained from the HHVV, HHHH, VVHH, and VVVV signals through the two different subtraction combinations given in Eq. (23).

dent probe polarization. For clarity, the acoustic responses are suppressed using a 10 ns Gaussian smoothing filter. The solid curves show the experimental data recorded with the analyzer polarization angles indicated. The dashed curves are calculated from the HHHH and HHVV signals using Eq. (5) The (45°,−45°) angle calculation corresponds rather well with the experimental curve. Note that the intensities of each pair of experimental and calculated signals were matched using a multiplicative correction factor. Remaining differences are likely due to the imperfect manual optimization of the heterodyne phases. In order to match the amplitudes of several signal traces in subtraction calculations, we have made use of the fact that at sufficiently long times, all anisotropic signal contributions have decayed, and only the polarization-independent thermal part of the signal remains. The signals were therefore equalized at their long time limits.

We note that the orientational signal is quite weak in comparison to the density signal, putting stringent requirements on the purity of the polarizations of all the beams. The most important technical problem is that unavoidably there are some optical components (windows, lens) between the input and output polarizers which partially depolarize the beam. As a result, the desired pure orientational signal, e.g., in the (45°,−45°) case, may be contaminated with depolarized density contributions. These were minimized by optimizing the phase of the reference beam and selectively amplifying the orientational contribution as much as possible. Still, some of our experimental (45°,−45°) data suffer from noise and the presence of spurious density signal contributions. The magnitudes of these contributions could be assessed readily by examining the intensity of any signal that
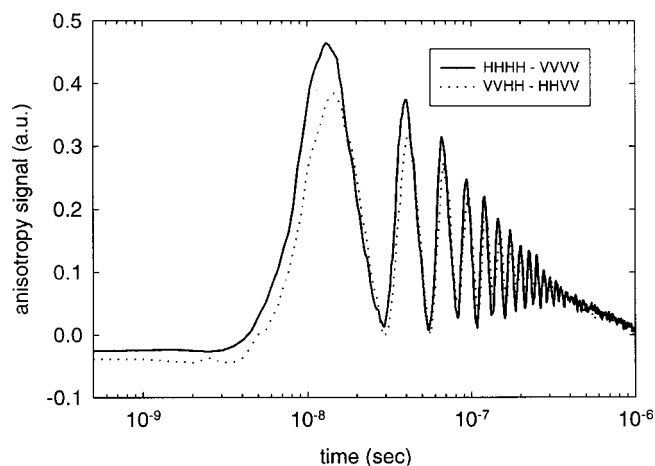
persisted at long delay times, after the orientational contributions had decayed and only density contributions remained.

Figure 7 illustrates the consistency between orientational contributions obtained by the different subtraction combinations given in Eq. (23). Figure 8 gives a similar illustration for density contributions to signal, calculated in the four different ways suggested by Eq. (23). The density and orientational signals shown in Figs. 7 and 8, respectively, are consistent with each other and with those determined directly through experiments at the corresponding magic angles (as already illustrated in Figs. 5 and 6).

In summary, the experimental results illustrate that the model and the approximations are reasonable for determination of both density and orientational contributions to ISTS data. Nevertheless, it is worthwhile to assess whether the omission of the stress-induced birefringence terms in Eq. (2), which are not due to molecular alignment, from the subsequent derivation could give rise to the small discrepancies observed or whether this approximation might introduce
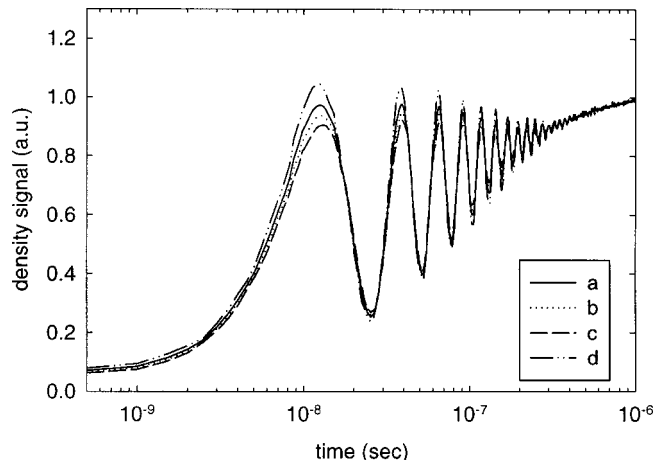

FIG. 8. Density response at 252 K, 52 μm grating spacing, obtained from the HHVV, HHHH, VVHH, and VVVV signals through the four different combinations given in Eq. (23). Signal combinations: (a) HHHH+2HHVV; (b) HHVV+VVHH+VVVV; (c) −HHHH+2VVHH+2VVVV; (d) 3HHHH+4HHVV−2VVHH−2VVVV.

other significant errors. For isotropic systems, the stress-induced birefringence terms can be written as[31]

$$\Delta n_{P,P} = \tfrac{1}{2} n_V^3 (q_{11} P_H + q_{12} P_V),$$
$$\Delta n_{P,\perp} = \tfrac{1}{2} n_V^3 (q_{12} P_H + q_{11} P_V),$$

(24)

such that the stress-induced birefringence is given by

$$\Delta n = \tfrac{1}{2} n_V^3 (q_{11} - q_{12})(P_H - P_V),$$

(25)

with P_H and P_V the density change related stresses in the horizontal and vertical direction, respectively, n_V the refractive index for vertically polarized light, and q_{11} and q_{12} the diagonal and off-diagonal characteristic elements of the photoelastic tensor, respectively. In general, q_{11} and q_{12} are different. In our experiment P_H and P_V are coupled to the density via the strain induced by the thermal expansion and horizontally propagating acoustic waves. The stress–strain relations for a longitudinal acoustic wave traveling in the horizontal direction[32]

$$P_H = P_{xx} = \rho v_L^2 \frac{\partial u}{\partial x} = \rho v_L^2 i q_L u_x,$$

$$P_V = P_{yy} = \rho v_L^2 \left[1 - \frac{2 v_T^2}{v_L^2} \right] \frac{\partial u}{\partial x} = \rho v_L^2 \left[1 - \frac{2 v_T^2}{v_L^2} \right] i q_L u_x,$$

(26)

with v_L and v_T the longitudinal and transverse acoustic velocity, respectively, and u the acoustic displacement, imply that the induced stress anisotropy increases with the time derivative of the density signal (via the wave vector $q_L = \omega / v_L$ and the horizontal displacement u_x) and the squared ratio between the shear and longitudinal velocity of the liquid. Although we do not have numerical values for the shear acoustic velocity of salol, for the main part of the temperature region of our study, this ratio is very small (e.g., in glycerol $v_T / v_L < 0.25$ for temperatures above the temperature of maximum relaxation[3,33]). The zero-frequency shear modulus is negligibly small at any temperature significantly above T_g, and the contribution to the gradual rise in signal (on microsecond time scales in the temperature range that we can measure it) also should be negligible. Only for the lowest temperatures may stress-induced birefringence start to play a role. For comparison, ISS measurements of shear and longitudinal acoustic waves (in a similar wave vector range) in the glass-forming liquid triphenylphospite[15] determined a shear acoustic velocity at the glass transition temperature (205 K) of about 1000 m/s for short wavelengths and a longitudinal acoustic velocity of about 2400 m/s, corresponding to $2 v_T^2 / v_L^2 = 0.35$. Typical values[34] for $(q_{11} - q_{12})$ for solids are between $10^{-12}\, \text{m}^2 \text{N}^{-1}$ and $5 \times 10^{-12}\, \text{m}^2 \text{N}^{-1}$. Combining these estimates results in stress-induced birefringence values between $3 \times 10^{-13}\, P_H$ and $10^{-12}\, P_H$. In our experiment the anisotropy contribution to the signal is typically about one-third of the signal, which, based on the calculated maximum relative refractive index signal variation of 4×10^{-7}, corresponds to about 1.3×10^{-7} birefringence variation and, using the Clausius–Mossotti relation,[35] to maximum strains of $\Delta \rho / \rho = 4 \times 10^{-7}$. Inserting this strain value in Eq. (26), one obtains maximum stresses P_H of about 14 kPa; and hence

maximum stress-induced birefringence values of the order of 10^{-8}, about ten times smaller than the anisotropy signal.

IV. SALOL DYNAMICS AND NONERGODICITY PARAMETER

Density and anisotropy response signals from salol covering a wide range of temperatures between 238 and 300 K have been collected and checked for consistency between the different methods of determination as illustrated above. Even for a single fixed grating spacing, the signals offer an abundance of information, as already illustrated in Yang *et al.*[4,5] Equation (13) illustrates that the density contribution renders thermal diffusivity, acoustic frequency, velocity, and damping rate, elastic modulus, structural relaxation amplitude, and characteristic structural relaxation time and stretching exponent. The orientational contribution, described by Eqs. (20) and (21), offers extra information about translation–rotation coupling, the characteristic orientational relaxation time, and the orientational decay stretching exponent. Since the orientational contribution to signal reflects the dynamics of both the orientational and density responses (the latter driving the former through flow), the orientational dynamics generally cannot be determined with high accuracy in ISTS measurements with typical signal/noise levels. In practice, OKE measurements represent a more straightforward method for extraction of orientational dynamics. It is noted that dynamic light scattering methods[26] with appropriate polarizations also permit determination of density and rotational signal contributions in supercooled liquids, and that the methods are often advantageous over complementary time and sample temperature ranges.

The strength of the orientational contributions to ISTS signals at any given polarization combination can be assessed with reasonable accuracy. This is important for analysis of the density response, which can be measured accurately through ISTS, and for determination of the translational–rotational coupling strength. Here, we focus on the amplitudes of the density and orientational contributions to signals and, for the density contributions, the relative amplitudes of the acoustic and steady-state signal levels from which the Debye–Waller factor can be determined.

Figure 9 shows typical experimental curves at 248, 256, and 270 K together with the best fits to Eq. (13) and Eq. (21). The initial rise time to reach the steady-state signal level, corresponding roughly to the characteristic density relaxation time, varies over several decades from about 8 ns at 270 K to about 700 ns at 248 K. At around 255 K (glass transition temperature $T_g = 218\, \text{K}$[6]) the damping rate for acoustic wavelength $\lambda = 52\, \mu\text{m}$ reaches its maximum value. This is the temperature region at which the characteristic density relaxation time τ_{st} is given by $\omega \tau_{st} \approx 1$. Generally, the density relaxation dynamics can be mapped out at slower time scales through the gradual nonexponential rise to the steady-state signal level and at faster times through the acoustic response including both the non-Lorentzian acoustic absorption spectrum and the corresponding dispersion in the acoustic velocity. Note that in the ISTS data shown in Fig. 9, the signal/noise ratio is reduced at times longer than 2 μs. This is a result of the use of two separate detectors for short and long
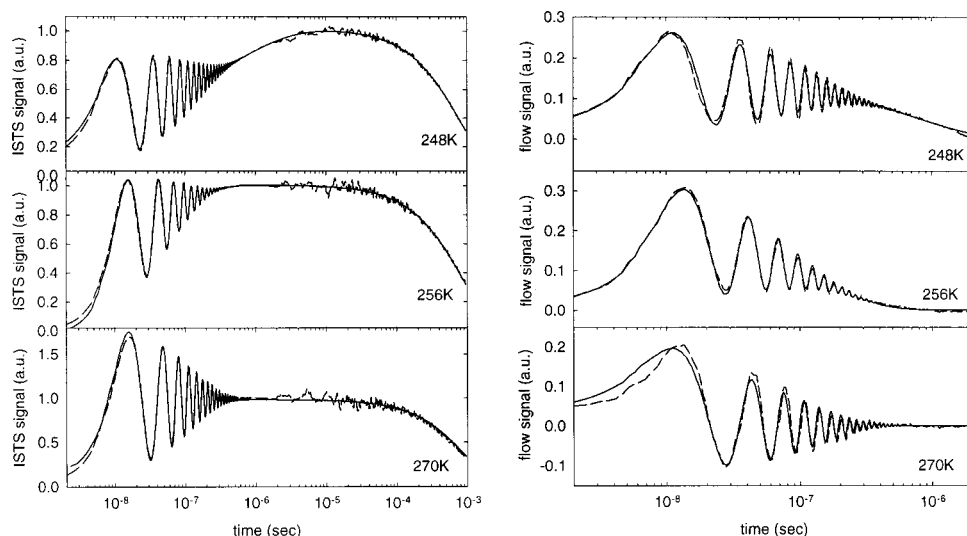
FIG. 9. Experimental data (dashed line) for density (left plot) and orientational responses (right plot) at 248, 256, and 270 K along with best fits (full line) using Eq. (13) for density and Eq. (20) for flow. The experimental response signals are averages over the four- and two-signal combinations, respectively, in Eq. (23) for the density and anisotropy signal.

time scales. The fast detector had very low electronic noise but was ac coupled, such that its filter response had to be deconvolved to correct the data traces at intermediate times. For long time scales a dc-coupled detector was used which had more electronic noise. The two parts of the signal were combined on the basis of a visually optimized amplification factor for one of them. In practice, the temporal overlap of data from the two detectors is sufficient to minimize the errors introduced by this process. Still, the uncertainties in stretching exponents, which are quite difficult to determine quantitatively, and in the relative amplitudes of acoustic and steady-state signal levels (needed below for determination of the Debye–Waller factor), are substantially greater than those of earlier measurements[4-6] for which a single low-noise detector was available.

The fitting convergence and quality were good overall, and the temperature dependences of the various fitting parameters support the results of Yang et al.,[4-6] who also obtained the wave vector dependence of the response and thus the dispersion characteristics of the acoustic moduli. Yang et al. analyzed their data as if they arose from pure density signals. We now know that this was not the case, so we must check to see whether the orientational contribution that was neglected may have biased the results of their structural relaxation data analysis. An important result from this analysis is the temperature dependence of the Debye–Waller factor, whose behavior was predicted by mode coupling theory (MCT). Figure 10 shows the present results along with the data and best fit to the MCT square-root prediction from Yang et al. The present result is consistent with that of Yang et al., in spite of their neglect of orientational effects. The values shown in Fig. 10 were determined through comparison between density contributions to acoustic and steady-state signals in the temperature range over which the condition $\tau_{ac} \ll \tau_{st} \ll \tau_{th}$ holds. Since the hydrodynamic quantities τ_{ac} and τ_{th} vary with wave vector, the temperature range was enlarged in the earlier work through measurements over a wide wave vector range. Although the present results are not sufficient for independent determination of the temperature-dependent behavior, it is clear that the Debye–Waller factor

values are not changed substantially by the inclusion of orientational effects in the analysis.

The temperature dependencies of the structural (density) and orientational relaxation times of the anisotropy signal in the high temperature range are shown in Fig. 11, and compared with relaxation times of Yang and Nelson[19] and Hinze et al.[2] Although the signal/noise ratios are not sufficient for accurate determination at all temperatures, the similarity between density and orientational relaxation times is clear. Our data provide approximate stretching exponents for the density at some temperatures, but given the complex orientational driving force and response, we cannot extract reliable values for an orientational stretching exponent. We show in Fig. 11 our results for these parameters along with the density values of Yang and Nelson[4,5] and the orientational values of Hinze et al.[2] The data also contain information about the temperature dependence of the rotational–translational coupling constant, in other words the strength of flow-induced orientation. Intuitively this coupling is related to viscosity and shear, and possible models have been reviewed.[25] As discussed earlier, the magnitude of the orientational signal
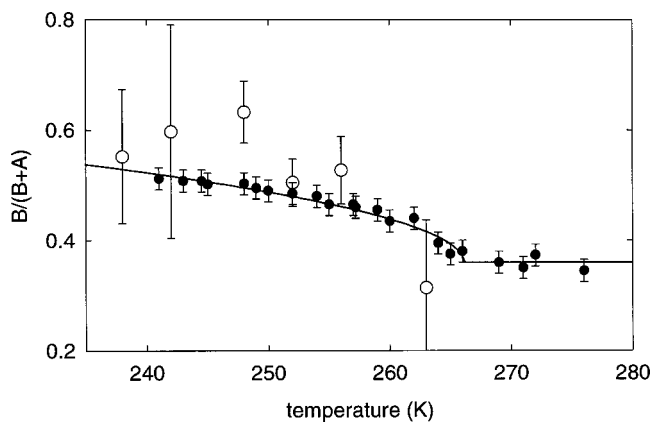

FIG. 10. Debye–Waller factor $B/(A+B)$ determined from the density relaxation amplitude B and relaxation-free amplitude A (open circles). The data (filled circles) and best modecoupling theoretical fit from Yang and Nelson (Refs. 4–6) are shown for comparison.
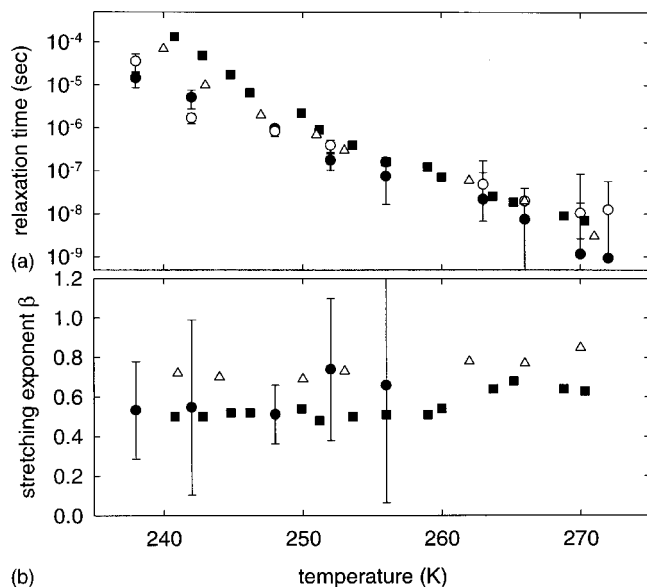
FIG. 11. (a) Characteristic decay times for density (filled circles) and anisotropy (open circles). (b) Stretching exponents for density (filled circles) for those temperatures at which reliable determination was possible. Orientational stretching exponents could not be determined reliably. The present results are included along with results of earlier ISTS (filled squares) and OKE-DIHARD (open triangles) measurements of the density and orientational responses, respectively.

depends also on the dynamics of the driving force, which makes the situation rather complicated for the long-time response because of strongly temperature-dependent relaxation dynamics. On the other hand, the dynamics of the oscillatory acoustic driving force do not vary greatly with temperature. The corresponding orientational response amplitude (normalized with the amplitude of the oscillatory density signal) is determined [as seen from Eq. (17) and Eq. (19)] by the product of a driving factor $\tau_{or}/\sqrt{f_{ac}^{-2}+(2\pi\tau_{or})^2}$ and the translation–rotation coupling constant. The experimental uncertainties, especially at low temperatures where the oscillation amplitudes in the data are small, make possible only an estimate of the temperature dependence of γ_{tr-rot}. The driving factor increases by a factor of approximately 2 as the temperature is reduced from 265 to 250 K (note that at the lower temperatures, τ_{or} becomes comparable with the acoustic oscillation period), indicating that γ_{tr-rot} remains almost temperature independent. This is consistent with calculated results of Kivelson *et al.*[12] (see Fig. 12).

V. CONCLUSIONS

The density and orientational contributions to ISTS measurements of supercooled liquid dynamics have been analyzed in detail theoretically and elucidated experimentally. Polarization combinations are prescribed that permit determination of the two contributions. Results from the supercooled liquid salol indicate that orientational contributions to signals are significant at both short times (during the acoustic oscillations) and longer times (during the gradual nonoscillatory evolution toward a steady-state response) at the temperatures we studied. The results show similar temperature-dependent trends in orientational and density dynamics.
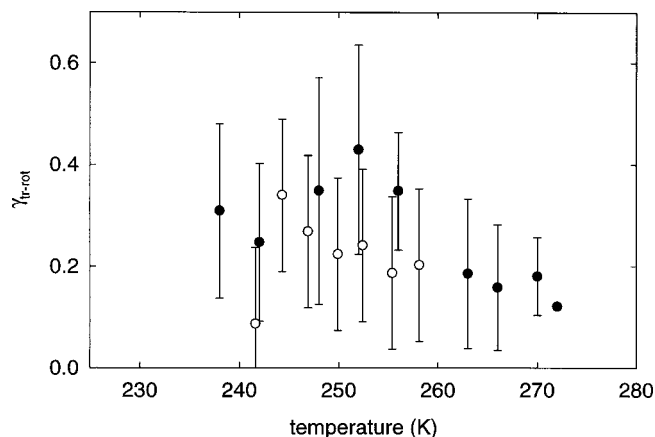

FIG. 12. Temperature dependence of the ratio of the oscillatory signal contributions due to flow-induced orientation and due to density. This ratio reflects the strength of translational–rotational coupling. The values were determined from the fits shown in Fig. 9. The full and open circles correspond to experimental data obtained with 52 μm, respectively, 16 μm grating spacing.

Previously reported conclusions that the Debye–Waller factor shows the temperature-dependent behavior predicted by mode-coupling theory, based on an analysis of ISTS results in which orientational contributions were neglected, were found to be valid even when the additional contributions are accounted for. ISTS measurements can be recorded with polarization combinations that exclude orientational contributions, in which case data analysis in terms of density responses only is justified.

The full analysis of ISTS data yields information about translational–rotational coupling and orientational relaxation dynamics in addition to acoustic properties and thermal responses from which density dynamics is deduced. Thus, an abundance of information is provided in a time window which is many orders of magnitude wide (ns–ms) and in a wave vector range of about two decades (corresponding to wavelengths of about 2–200 microns). The information provided within these ranges offers insight into viscoelastic responses throughout the supercooled liquid region.

[1] G. Hinze, D. D. Brace, S. D. Gottke, and M. D. Fayer, Phys. Rev. Lett. **84**, 2437 (2000).
[2] G. Hinze, R. S. Francis, and M. D. Fayer, J. Chem. Phys. **111**, 2710 (1999).
[3] Y. X. Yan, L. T. Cheng, and K. A. Nelson, J. Chem. Phys. **88**, 6477 (1988).
[4] Y. Yang and K. A. Nelson, J. Chem. Phys. **103**, 7722 (1995).
[5] Y. Yang and K. A. Nelson, J. Chem. Phys. **103**, 7732 (1995).
[6] Y. Yang and K. A. Nelson, Phys. Rev. Lett. **74**, 4883 (1995).
[7] R. Torre, P. Bartolini, and R. M. Pick, Phys. Rev. E **57**, 1912 (1998).

[8] G. Hinze, D. D. Brace, S. D. Gottke, and M. D. Fayer, J. Chem. Phys. **113**, 3723 (2000).

[9] W. Köhler, G. Fytas, W. Steffen, and L. Reinhardt, J. Chem. Phys. **104**, 248 (1996).

[10] R. Torre, P. Bartolini, M. Ricci, and R. Pick, Europhys. Lett. **52**, 324 (2000).

[11] R. Elschner, R. Macdonald, H. J. Eichler, S. Hess, and A. M. Sonnet, Phys. Rev. E **60**, 1792 (1999).

[12] D. Kivelson, T. Keyes, and J. Champion, Mol. Phys. **31**, 221 (1976).

[13] K. A. Nelson, R. Casalegno, R. J. D. Miller, and M. D. Fayer, J. Chem. Phys. **77**, 1144 (1982).

[14] F. W. Deeg and M. D. Fayer, J. Chem. Phys. **91**, 2269 (1989).

[15] S. M. Silence, A. R. Duggal, L. Dhar, and K. A. Nelson, J. Chem. Phys. **96**, 5448 (1992).

[16] K. A. Nelson, R. J. D. Miller, D. R. D. R. Lutz, and M. D. Fayer, J. Appl. Phys. **53**, 1144 (1982).

[17] G. Eyring and M. D. Fayer, J. Chem. Phys. **81**, 4314 (1984).

[18] T. F. Crimmins, A. A. Maznev, and K. A. Nelson, Appl. Phys. Lett. **74**, 1344 (1999).

[19] A. A. Maznev, K. A. Nelson, and J. A. Rogers, Opt. Lett. **23**, 1319 (1998).

[20] W. Götze and L. Sjögren, Rep. Prog. Phys. **55**, 241 (1992).

[21] R. D. Mountain, J. Res. Natl. Bur. Stand., Sect. A **70**, 207 (1966).

[22] R. D. Mountain, J. Res. Natl. Bur. Stand., Sect. A **72**, 95 (1968).

[23] R. Böhmer, K. L. Ngai, and C. A. Angell, J. Chem. Phys. **99**, 4201 (1993).

[24] W. Götze, J. Phys.: Condens. Matter **11**, A1 (1999).

[25] N. C. Hilyard and H. G. Jerrard, J. Appl. Phys. **33**, 3470 (1962).

[26] B. J. Berne and R. Pecora, *Dynamic Light Scattering* (Wiley, New York, 1976).

[27] H. J. Eichler, P. Gunter, and D. W. Pohl, *Laser-induced Dynamic Gratings* (Springer, Berlin, 1986).

[28] J. Machta, I. Oppenheim, and I. Procaccia, Phys. Rev. Lett. **42**, 1368 (1979).

[29] I. Procaccia, D. Ronis, M. A. Collins, J. Ross, and I. Oppenheim, Phys. Rev. A **19**, 1290 (1979).

[30] D. Ronis, I. Procaccia, and I. Oppenheim, Phys. Rev. A **19**, 1324 (1979).

[31] M. Born and E. Wolf, *Principles of Optics, Electromagnetic Theory of Propagation, Interference and Diffraction of Light*, 7th ed. (Cambridge University Press, Cambridge, UK, 1999).

[32] J. D. Achenbach, *Wave Propagation in Elastic Solids* (Elsevier Science, Amsterdam, 1993), Vol. 16.

[33] R. Picirelli and T. A. Litovitz, J. Acoust. Soc. Am. **29**, 1009 (1957).

[34] W. R. J. Cook and H. Jaffe, *American Institute of Physics Handbook*, 3rd ed. (McGraw-Hill, New York, 1972).

[35] N. W. Ashcroft and N. D. Mermin, *Solid State Physics* (Saunders College Publishing, Philadelphia, 1976).